



Scaling of small-scale wall turbulence

S.L. Tang^{1,†} and R.A. Antonia²

¹Center for Turbulence Control, Harbin Institute of Technology, Shenzhen 518055, PR China

²School of Engineering, University of Newcastle, NSW 2308, Australia

(Received 29 January 2022; revised 19 June 2022; accepted 13 August 2022)

In the vicinity of walls, turbulence is anisotropic. Since the classical hypotheses of Kolmogorov (*Dokl. Akad. Nauk SSSR*, vol. 30, 1941, pp. 299–303), Obukhov (*Izv. Akad. Nauk SSSR Geogr. Geofiz.*, vol. 13, 1949, pp. 58–69) and Corrsin (*J. Appl. Phys.*, vol. 22, 1951, pp. 469–473) require small-scale turbulence to be isotropic, they have only limited relevance to wall-bounded turbulent flows. Here, we put forward a hypothesis whereby small-scale near-wall statistics, when suitably normalized, are independent of the type of flow as well as of the Reynolds and Péclet numbers. The relatively large amount of available wall turbulence direct numerical simulations data, related mainly to second-order statistics, in a channel flow and a boundary layer provides good support for the independence with respect to the Reynolds number. To fully validate the hypothesis, more data are required for higher-order statistics as well as for other wall flows and for different surface conditions.

Key words: turbulence theory

1. Introduction

One striking success in describing and predicting small-scale turbulent motion (Nelkin 1992) is the phenomenological picture for the velocity field introduced by Kolmogorov (1941). Kolmogorov's hypotheses were extended further by Obukhov (1949) and Corrsin (1951) to describe the behaviour of a passive scalar field within a turbulent flow. The Kolmogorov–Obukhov–Corrsin hypotheses are commonly referred to as the KOC theory in the literature. This theory requires that the Reynolds and Péclet numbers are sufficiently large so that the small-scale velocity and passive scalar fields are isotropic and statistically independent of the large scales (Warhaft 2000; Chassaing *et al.* 2002). However, wall turbulent flows are characterized by anisotropy (Antonia, Kim & Browne 1991; Kasagi, Tomita & Kuroda 1992; Antonia, Abe & Kawamura 2009; Vreman & Kuerten 2014*a,b*; Tang *et al.* 2015; Pumir, Xu & Siggia 2016; Kaneda & Yamamoto 2021), especially near

† Email address for correspondence: shunlin.tang88@gmail.com

the wall, thus the influence of the large scales on small-scale quantities may persist. Wall turbulence is of great importance in meteorological and oceanic flows and hence in a climatological context (Marusic, Mathis & Hutchins 2010; Smits & Marusic 2013). The flow behaviour in the near-wall region also determines the drag force on planes and ships, and the energy required to pump fluids through pipelines (Marusic *et al.* 2010; Smits & Marusic 2013). Pipe and channel flows and the boundary layer, including the atmospheric surface layer, are the most frequently investigated wall-bounded turbulent flows. The conventional scaling of wall turbulence is based on the wall parameters u_τ , θ_τ and ν , where $u_\tau = (\tau_w/\rho)^{1/2}$ is the friction velocity (τ_w is the wall shear stress and ρ is the density of the fluid), ν is the kinematic viscosity, and $\theta_\tau = Q_w/\rho c_p u_\tau$ is the friction temperature (Q_w is the averaged wall heat flux and c_p the specific heat at constant pressure). Several decades of research into small-scale wall turbulence have shown that the scaling of small-scale quantities, such as the mean turbulent energy dissipation rate $\bar{\varepsilon}$ ($\equiv \overline{v(\partial u_i/\partial x_k)(\partial u_i/\partial x_k)}$), the mean scalar dissipation rate $\bar{\varepsilon}_\theta$ ($\equiv \overline{\kappa(\partial\theta/\partial x_k)(\partial\theta/\partial x_k)}$) and their transport equations, based on u_τ , θ_τ and ν , is untenable in the region near the wall (Antonia *et al.* 1991; Kasagi *et al.* 1992; Antonia & Kim 1994; Abe, Antonia & Kawamura 2009; Vreman & Kuerten 2014*b*; Gerolymos & Vallet 2016; Alcántara-Ávila, Hoyas & Pérez-Quiles 2021; Pirozzoli *et al.* 2021). The scaling of the energy spectra based on u_τ and ν near the wall is also untenable (see figure 5(a), which will be discussed later). Here, the streamwise (x_1), wall-normal (x_2) and spanwise (x_3) velocity fluctuations are denoted respectively by u_1 , u_2 and u_3 . Also, κ is the thermal diffusivity, θ denotes the scalar fluctuation, and the overbar denotes an averaged value at a given x_2 location. To our knowledge, there is no theory that can describe and predict the behaviour of small-scale wall turbulence. The major objective of this paper is to develop a hypothesis that addresses this behaviour in an adequate manner.

2. A hypothesis of small-scale wall turbulence

If a proper theory of small-scale wall turbulence were to emerge, which has the prospect of being universal, then it first requires the identification of the proper scaling parameters for small-scale quantities, which, as noted above, are unlikely to be the conventional scaling of wall turbulence, i.e. u_τ , θ_τ and ν . Another set of scaling parameters for small-scale turbulence provided by the KOC theory is $\bar{\varepsilon}$, $\bar{\varepsilon}_\theta$ and ν . This requires local isotropy to be satisfied and the small scales to be statistically independent of the large scales. These two requirements are not satisfied in wall turbulence (Antonia *et al.* 1991, 2009; Kasagi *et al.* 1992; Abe *et al.* 2009; Vreman & Kuerten 2014*a,b*; Tang *et al.* 2015; Gerolymos & Vallet 2016; Pumir *et al.* 2016; Alcántara-Ávila *et al.* 2021; Kaneda & Yamamoto 2021), so the theory is invalidated. In wall turbulence, one expects that the small scales will deviate from isotropy and may be affected by the large-scale forcing associated with diffusion and mean shear phenomena. However, if this deviation and the effect of the large-scale forcing can become independent of the Reynolds and Péclet numbers, then the small-scale quantities, when suitably normalized, may become universal. If $\bar{\varepsilon}$, $\bar{\varepsilon}_\theta$ and ν are indeed the proper scaling parameters, then we can formulate a hypothesis for small-scale wall turbulence, as follows.

In wall turbulence at sufficiently high Reynolds and Péclet numbers, although the effect of the large-scale forcing on the small scales depends on the distance from the wall and on the turbulent scale (or wavenumber), it does not depend on the Reynolds and Péclet numbers when the normalization uses $\bar{\varepsilon}$, $\bar{\varepsilon}_\theta$ and ν . Consequently, the small-scale statistics are universal. They depend only on the turbulent scale (or wavenumber) and the distance

from the wall. The larger the Reynolds and Péclet numbers, the larger the distance from the wall and the range of turbulent scales over which this universality applies. By ‘universality’ we mean independence with respect to the type of flow as well as the Reynolds and Péclet numbers.

Mathematically, this hypothesis predicts that in wall turbulence, the behaviour of any small-scale quantity, say Ψ , can be expressed as

$$\Psi(r^* \text{ or } k^*, x_2^*) = f_\Psi(r^* \text{ or } k^*, x_2^*), \quad (2.1)$$

where the asterisk denotes normalization by $\bar{\varepsilon}$, $\bar{\varepsilon}_\theta$ and ν (or equivalently the Batchelor temperature scale $\theta_B = (\bar{\varepsilon}_\theta(\nu/\bar{\varepsilon})^{1/2})^{1/2}$ and the Kolmogorov velocity $u_K = (\nu\bar{\varepsilon})^{1/4}$ and length $\eta = (\nu^3/\bar{\varepsilon})^{1/4}$ scales), and the function f_Ψ is universal; f_Ψ should depend only on x_2^* and the scale r^* in physical space (or wavenumber k^* in spectral space) once appropriate values of the Reynolds and Péclet numbers are reached. In particular, at a given scale r^* (or k^*) in the small-scale range, $\Psi(x_2^*)$ will depend only on x_2^* . We immediately recover the predictions of the KOC theory, provided that local isotropy is satisfied and the small scales are statistically independent of the large scales in the region far from the wall, *viz.* $\Psi(r^* \text{ or } k^*) = f_\Psi(r^* \text{ or } k^*)$; this is supported by the energy spectra in a channel flow, in a boundary layer and in a pipe flow (Saddoughi & Veeravalli 1994; Rosenberg *et al.* 2013; Tang *et al.* 2015; Vallikivi, Ganapathisubramani & Smits 2015). Further, for scales larger than the viscous scales but smaller than the integral scale L (representing the scale at which turbulent energy is introduced), the KOC theory predicts that $\Psi(r \text{ or } k)$ are uniquely determined by $\bar{\varepsilon}$ and $\bar{\varepsilon}_\theta$ (no longer depending on ν). In this case, a universal scaling law, *i.e.* the Kolmogorov $k^{-5/3}$ scaling of the energy spectrum, emerges. This is supported by the spectra of Rosenberg *et al.* (2013) on the pipe centreline at $Re_\tau = 98\,190$, where one can observe approximately one decade of $k^{-5/3}$ behaviour. Evidently, the KOC predictions are compatible with those of the present hypothesis provided that the distance from the wall is sufficiently large, local isotropy is satisfied, and the small scales are statistically independent of the large scales. However, when the latter conditions do not apply, the present hypothesis extends the KOC theory in a significant way.

3. Test of the hypothesis

Figure 1(a) shows the distributions of $\bar{\varepsilon}^+$, where $+$ denotes normalization by u_τ and ν , in a channel flow over a large range of Re_τ (550–10⁴). Since $\bar{\varepsilon}^+ = u_K^4/u_\tau^4 = \delta_v^4/\eta^4$, the purpose of showing the $\bar{\varepsilon}^+$ distributions is to examine whether they can collapse over a certain x_2^+ range. This would imply that the wall parameters and the Kolmogorov scales can be used interchangeably in this range. In the region $x_2^+ \lesssim 20$, the magnitude of $\bar{\varepsilon}^+$ increases systematically with Re_τ . Beyond this region, it decreases quickly with x_2^+ to approach a value close to 0 at $x_2^+ \approx 10^3$. In order to examine this region more closely, figure 1(b) shows the same distributions premultiplied by x_2^+ , *i.e.* $x_2^+\bar{\varepsilon}^+$; note that this does not affect the collapse of $\bar{\varepsilon}^+$, if it indeed exists. Evidently, the magnitude of $x_2^+\bar{\varepsilon}^+$ evolves systematically with Re_τ except for the distributions at $Re_\tau = 5200$ and 10^4 , which collapse over the range $50 \lesssim x_2^+ \lesssim 200$. Further, the distributions of $x_2^+\bar{\varepsilon}^+$ in figure 1(b) do not exclude the possibility that the x_2^+ range over which $x_2^+\bar{\varepsilon}^+$ collapses may extend to larger and smaller values of x_2^+ as Re_τ keeps increasing. In particular, we underline that if $x_2^+\bar{\varepsilon}^+$ does not collapse, then scaling based on Kolmogorov scales will exclude the scaling based on wall parameters, and vice versa.

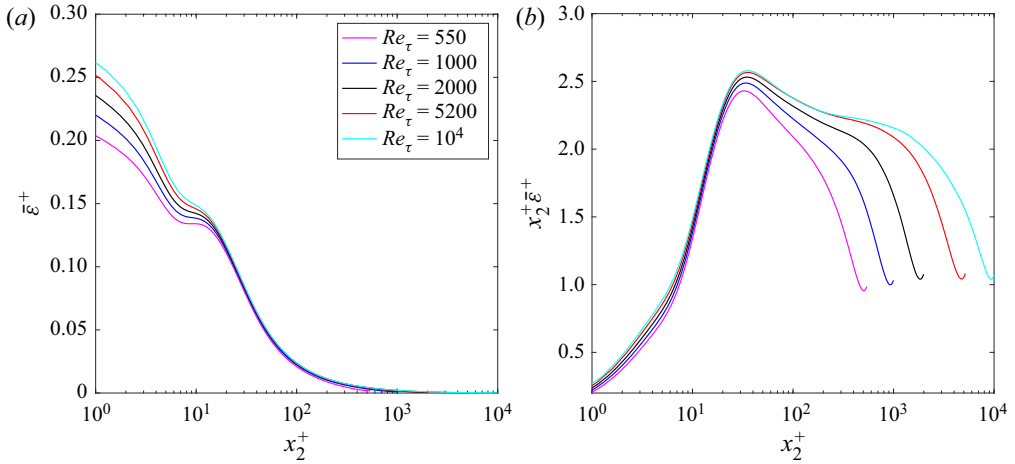


Figure 1. Distributions of (a) $\bar{\epsilon}^+$ and (b) $x_2^+ \bar{\epsilon}^+$ in a channel flow. They are plotted using the data of Lee & Moser (2015, 2019) and Hoyas *et al.* (2022).

Before testing the scaling based on the Kolmogorov scales, we report in figure 2 the variation of x_2^* with x_2^+ across the whole channel, over the ranges $x_2^+ = 0-100$ and $x_2^+ = 1-3$, respectively. This figure helps to identify the x_2^+ range that corresponds to the x_2^* range over which the present hypothesis applies. Note that $x_2^* = x_2^+/\eta^+ = x_2^+ \bar{\epsilon}^{+1/4}$. Strictly speaking, at a given x_2^+ , if $\bar{\epsilon}^+$ (or equivalently $x_2^+ \bar{\epsilon}^+$) does not collapse (figure 1), then x_2^* also should not collapse. Indeed, the dependence of x_2^* on Re_τ at a given x_2^+ can be observed from figures 2(a,b) and the inset, at large x_2^+ ($\gtrsim 500$), moderate x_2^+ (~ 100) and small x_2^+ (~ 1). We first test the scaling based on the wall parameters and the Kolmogorov scales in the context of the components of the dissipation rate tensor, i.e.

$$R_1 = 2\nu \overline{\left(\frac{\partial u_1}{\partial x_k} \frac{\partial u_1}{\partial x_k} \right)}, \quad R_2 = 2\nu \overline{\left(\frac{\partial u_2}{\partial x_k} \frac{\partial u_2}{\partial x_k} \right)}, \quad R_3 = 2\nu \overline{\left(\frac{\partial u_3}{\partial x_k} \frac{\partial u_3}{\partial x_k} \right)}. \quad (3.1a-c)$$

Since $R_1 + R_2 + R_3 = 2\bar{\epsilon}$, we show, as in figure 1(b), the premultiplied R_i^+ in figure 3(a), i.e. $x_2^+ R_i^+$ for $Re_\tau = 550-10^4$. The distributions of R_i^* are plotted in figure 3(b). The following comments can be made with regard to figure 3. (i) Like the distributions of $x_2^+ \bar{\epsilon}^+$, those of $x_2^+ R_i^+$ also collapse approximately at $Re_\tau = 5200$ and 10^4 in the range $50 \lesssim x_2^+ \lesssim 200$. (ii) In the region $x_2^+ \lesssim 10$, $x_2^+ R_2^+ \approx 0$ and thus the collapse is not surprising. (iii) In the region around $x_2^+ \approx 23$, there is a reasonably good collapse for $x_2^+ R_1^+$ at all Re_τ . Since $x_2^+ (R_1^+ + R_2^+ + R_3^+) = 2x_2^+ \bar{\epsilon}^+$ and the $x_2^+ \bar{\epsilon}^+$ distributions around $x_2^+ \approx 23$ do not collapse (see figure 1b), the collapse of $x_2^+ R_1^+$ around this location implies a relatively more rapid evolution for other components, which is indeed observed from the $x_2^+ R_3^+$ distributions. (iv) Except for the quantities at certain locations, as mentioned above, the other distributions evolve systematically with Re_τ . (v) In contrast, there is a nearly perfect collapse for the distributions of R_2^* across the channel when $Re_\tau > 1000$. The same feature can be observed in the R_1^* and R_3^* distributions when $Re_\tau > 1000$ and $x_2^* \gtrsim 20$. (vi) In the region $x_2^* \lesssim 20$, the magnitudes of R_1^* and R_3^* appear to evolve, albeit slightly, with Re_τ for $Re_\tau \gtrsim 550$. This is consistent with the observation, also in a channel flow, of Gerolymos & Vallet (2016) that the peaks of $R_1/(2\bar{\epsilon}) - 1/3$ and $R_3/(2\bar{\epsilon}) - 1/3$ vary with Re_τ . However, a close look at the distributions of R_1^* and R_3^* in the region $x_2^* \lesssim 20$ shows that there is

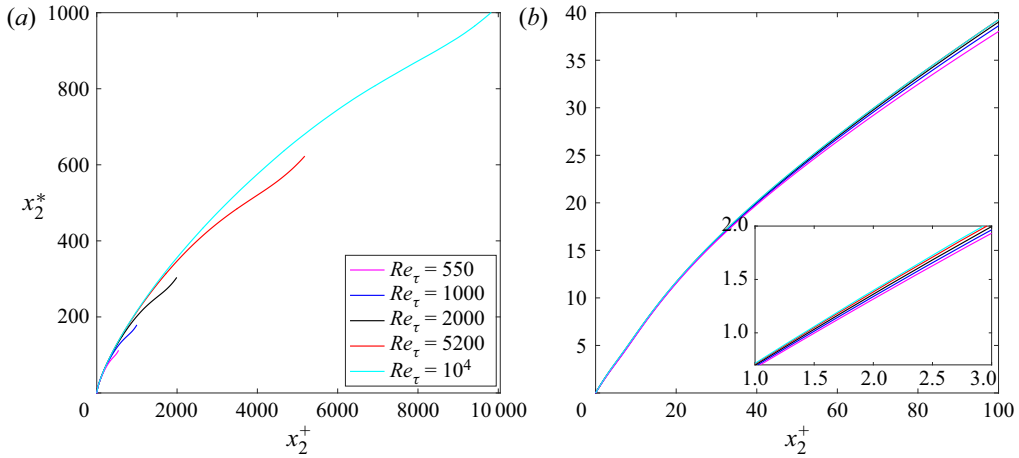


Figure 2. Variation of x_2^* with x_2^+ (a) across the whole channel and (b) on the range $x_2^+ = 0-100$. The inset in (b) zooms in on the range $x_2^+ = 1-3$. The plots use the data of Lee & Moser (2015, 2019) and Hoyas *et al.* (2022).

an approximate collapse when $Re_\tau > 1000$; this is confirmed by figure 4, which shows the distributions of R_1^* , R_2^* and R_3^* for $Re_\tau > 1000$ in the channel flow. Note that the same feature can be observed also in the distributions of the Kolmogorov-normalized $R_{12} = 2\nu((\partial u_1/\partial x_k)(\partial u_2/\partial x_k))$, i.e. R_{12}^* , which are also shown in figure 4. (vii) Overall, the comparison between the wall-parameter-normalized and Kolmogorov-normalized distributions of R_i indicates that the scaling based on Kolmogorov scales is superior to that based on wall parameters. More importantly, there is an approximate collapse for all distributions across the channel when $Re_\tau > 1000$ (figure 4). Also shown in figure 4 are the R_i^* and R_{12}^* distributions in a boundary layer for $Re_\tau > 1000$. It is remarkable that the boundary layer data can collapse reasonably well with the channel data in the region $x_2^* \lesssim 70$. Evidently, figure 4 provides reasonably good support for the present small-scale wall turbulence hypothesis.

Before testing the hypothesis systematically in the context of energy spectra, it is desirable to compare the wall-parameter- and Kolmogorov-normalized spectra at a location very near the wall to evaluate which scaling is adequate. The results are shown in figures 5(a,b), which compare the wall-parameter-normalized spectrum $\phi_{u_2}(k_{x_3}^+)$ at $x_2^+ = 2$ with the Kolmogorov-normalized spectrum $\phi_{u_2}(k_{x_3}^*)$ at $x_2^* = 1.5$ in a channel flow (Lee & Moser 2015, 2019). The comparison allows a critical evaluation of the two normalizations, using exaggerated horizontal and vertical axes. The same scales for the horizontal axis and two decades for the vertical axis are used in figures 5(a,b). These two locations ($x_2^+ = 2$ and $x_2^* = 1.5$) are close to each other (see the inset of figure 2b). It can be seen that there is no collapse for $\phi_{u_2}(k_{x_3}^+)$, regardless of the wavenumber. Instead, the variation of $\phi_{u_2}(k_{x_3}^+)$ with Re_τ is systematic, implying that the scaling based on wall parameters is not tenable. In contrast, there is a good collapse for $\phi_{u_2}(k_{x_3}^*)$ in the high-wavenumber range (small-scale range). This is consistent with the prediction of the present hypothesis.

We now test the hypothesis using spectra in both a channel flow and a boundary layer. According to (2.1), the spectra should be universal in the small-scale range, depending only on x_2^* and k^* . In particular, at a given distance x_2^* from the wall, energy spectra should depend only on k^* . Figure 6 shows the Kolmogorov-normalized $\phi_{u_1}(k_{x_3}^*)$, $\phi_{u_2}(k_{x_3}^*)$ and

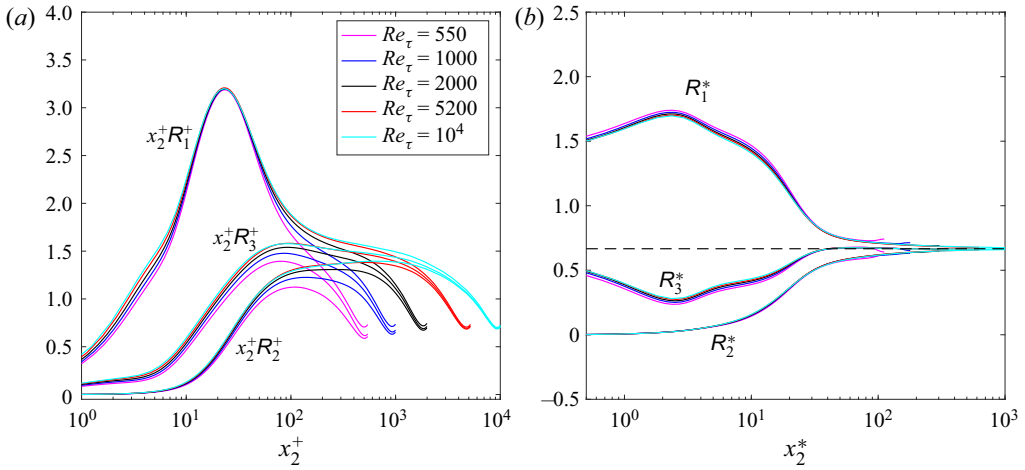


Figure 3. Distributions of R_1 , R_2 and R_3 in a channel flow. Normalizations based on (a) wall parameters and (b) Kolmogorov scales. They are plotted using the data of Lee & Moser (2015, 2019) and Hoyas *et al.* (2022). Note that the R_i^+ distributions in (a) have been premultiplied by x_2^+ . The horizontal line in (b) indicates the isotropic ratio (2/3).

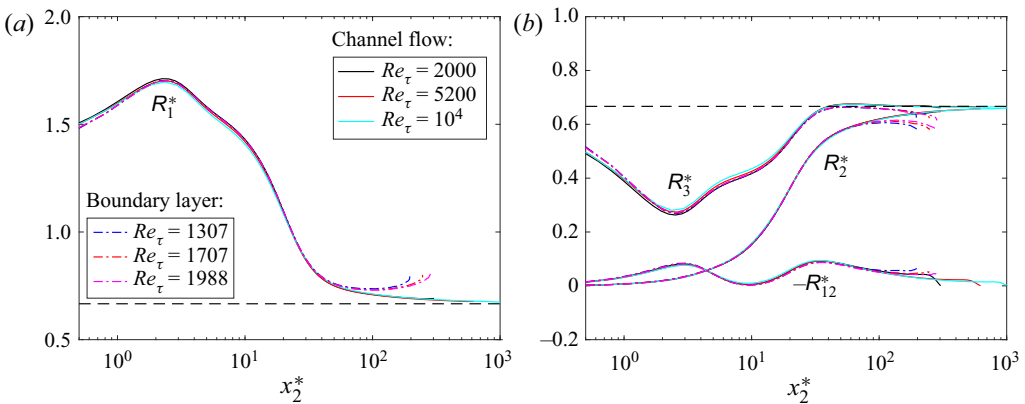


Figure 4. Distributions of (a) R_1^* , and (b) R_2^* and R_3^* , in a channel flow for $Re_\tau > 1000$ for the data in figure 3(b); the corresponding distributions for the Kolmogorov-normalized $R_{12} = 2\nu((\partial u_1/\partial x_k)(\partial u_2/\partial x_k))$, i.e. R_{12}^* , are also shown. For comparison, the boundary data of Simens *et al.* (2009), Jiménez *et al.* (2010), Borrell, Sillero & Jiménez (2013) and Sillero, Jiménez & Moser (2013) for $Re_\tau > 1000$ are also shown. Note that as in figures 9(a) and 10(a), the data close to and beyond the edge of the boundary layer ($x_2/\delta > 0.8$) are not shown since they are affected by the intermittency associated with the turbulent/potential flow interface.

$\phi_{u_3}(k_{x_3}^*)$ at $x_2^* = 1.5$ in a channel flow and a boundary layer. At this very-near-wall location, all spectra collapse reasonably well in the small-scale range, except for $\phi_{u_1}(k_{x_3}^*)$, which requires $Re_\tau \gtrsim 1000$ for $\phi_{u_1}(k_{x_3}^*)$ to collapse over a large range of $k_{x_3}^*$. This implies that the threshold value of Re_τ , beyond which the hypothesis is valid, may depend on the specific quantity investigated. For this reason, the spectra of u_1 in both the x_1 and x_3 directions at $Re_\tau = 550$ will not be shown in figures 7–9. When $Re_\tau \gtrsim 1000$, the collapse of $\phi_{u_1}(k_{x_3}^*)$ and $\phi_{u_3}(k_{x_3}^*)$ extends to $k_{x_3}^* \approx 0.015$ and 0.05, respectively. In contrast, there is adequate collapse at virtually all wavenumbers for $\phi_{u_2}(k_{x_3}^*)$ over the same range of $Re_\tau (\gtrsim 1000)$.

Scaling of small-scale wall turbulence

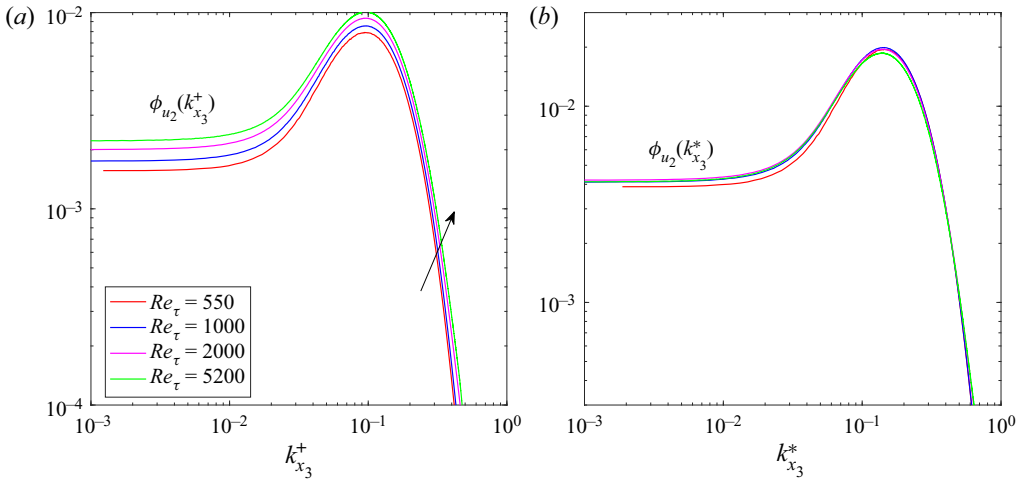


Figure 5. (a) Wall parameter-normalized spectrum $\phi_{u_2}(k_{x_3}^+)$ at $x_2^+ = 2$ in a channel flow (Lee & Moser 2015, 2019). The arrow is in the direction of increasing Re_τ . (b) Kolmogorov-normalized spectra at $x_2^* = 1.5$, which is close to $x_2^+ = 2$ (see the inset in figure 2b). Note that when data were not obtained at exactly $x_2^+ = 2$ and $x_2^* = 1.5$, interpolation was used, based on available spectra closest to these two locations.

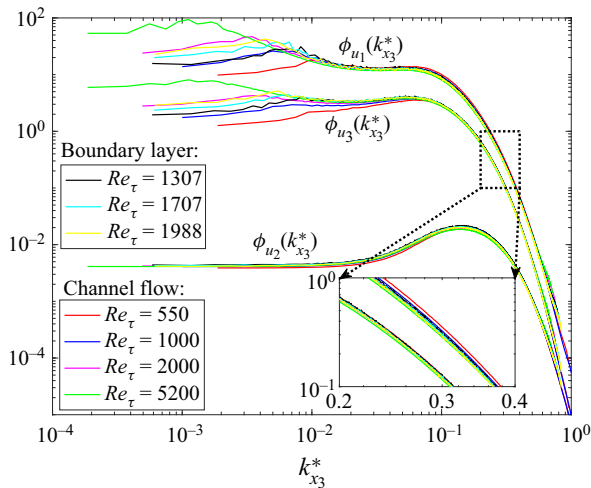


Figure 6. Kolmogorov-normalized spectra at $x_2^* = 1.5$ in a channel flow and a boundary layer. The inset zooms in on the range $k_{x_3}^* = 0.2$ – 0.4 for $\phi_{u_1}(k_{x_3}^*)$ and $\phi_{u_3}(k_{x_3}^*)$. Note that when data were not obtained at exactly $x_2^* = 1.5$, interpolation was used, based on available spectra closest to this location.

Figures 7(a,b) show distributions of $\phi_{u_1}(k_{x_3}^*)$, $\phi_{u_2}(k_{x_3}^*)$ and $\phi_{u_3}(k_{x_3}^*)$ in a channel flow and a boundary layer at two locations ($x_2^* = 10$ and 50) over a wide range of $Re_\tau (= 550$ – $5200)$. Figures 8(a,b) show distributions of $\phi_{u_1}(k_{x_1}^*)$, $\phi_{u_2}(k_{x_1}^*)$ and $\phi_{u_3}(k_{x_1}^*)$ in a channel flow at the same locations. As expected, the collapse is nearly perfect over a wide range of relatively large wavenumbers after normalizing by the Kolmogorov scales (or equivalently, $\bar{\varepsilon}$ and ν). When $Re_\tau \gtrsim 1000$, the collapse of $\phi_{u_1}(k_{x_3}^*)$, $\phi_{u_2}(k_{x_3}^*)$ and $\phi_{u_3}(k_{x_3}^*)$ extends to $k_{x_3}^* \approx 0.02$, 0.1 and 0.05 , respectively, at $x_2^* = 10$ (figure 7a). At a location further away from the wall ($x_2^* = 50$, figure 7b), the collapse of $\phi_{u_1}(k_{x_3}^*)$, $\phi_{u_2}(k_{x_3}^*)$ and $\phi_{u_3}(k_{x_3}^*)$ can

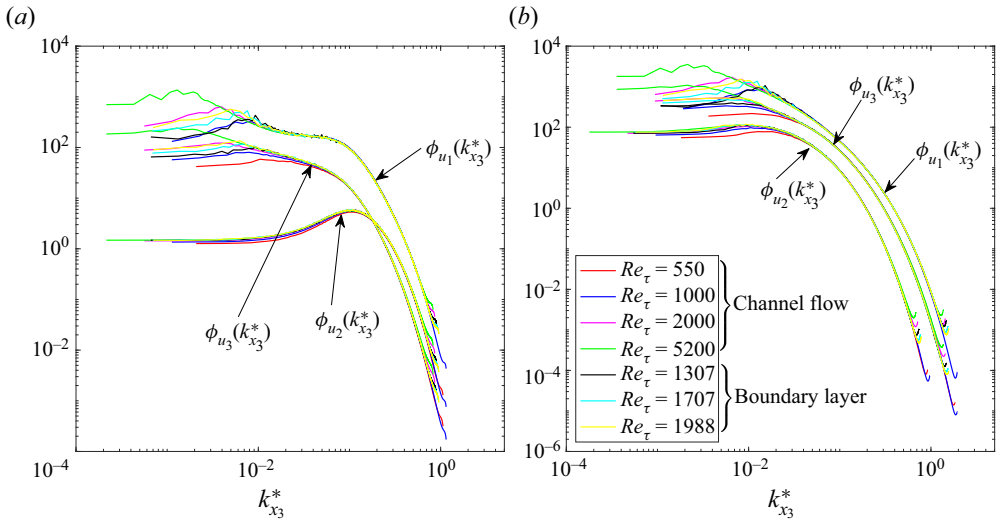


Figure 7. Energy spectra in a boundary layer and a channel flow. Distributions of $\phi_{u_1}(k_{x_3}^*)$, $\phi_{u_2}(k_{x_3}^*)$ and $\phi_{u_3}(k_{x_3}^*)$ at (a) $x_2^* = 10$ and (b) $x_2^* = 50$. The plots use the wall-parameter-normalized spectra in a boundary layer (Simens *et al.* 2009; Jiménez *et al.* 2010; Borrell *et al.* 2013; Sillero *et al.* 2013) and the non-normalized spectra in a channel flow (Lee & Moser 2015, 2019). For clarity, the distributions at $x_2^* = 50$ for $\phi_{u_2}(k_{x_3}^*)$ in (b) are shifted to the left by 0.5 of a decade. Note that the spectrum of u_1 at $Re_\tau = 550$ is not shown for the reason mentioned in the context of figure 6. Note also that when data were not obtained at exactly $x_2^* = 10$ and 50, interpolation was used, based on available spectra closest to these two locations.

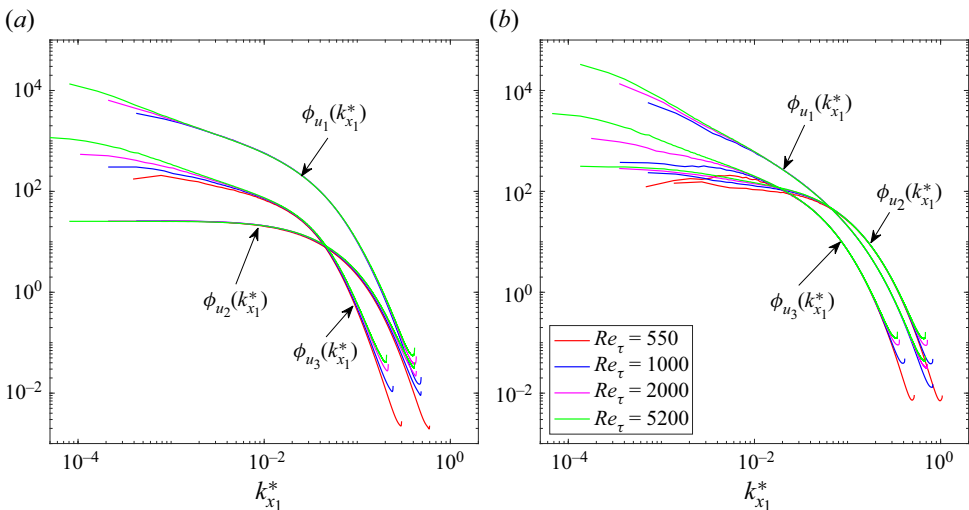


Figure 8. Energy spectra in a channel flow. Distributions of $\phi_{u_1}(k_{x_1}^*)$, $\phi_{u_2}(k_{x_1}^*)$ and $\phi_{u_3}(k_{x_1}^*)$ at (a) $x_2^* = 10$ and (b) $x_2^* = 50$. The plots use the non-normalized spectra in a channel flow (Lee & Moser 2015, 2019). For clarity, the distributions for $\phi_{u_3}(k_{x_1}^*)$ in (a,b) are shifted to the left by 0.5 of a decade. Note that the spectrum of u_1 at $Re_\tau = 550$ is not shown in (a,b) for the reason mentioned in the context of figure 6. Note also that when data were not obtained at exactly $x_2^* = 10$ and 50, interpolation was used, based on available spectra closest to these two locations.

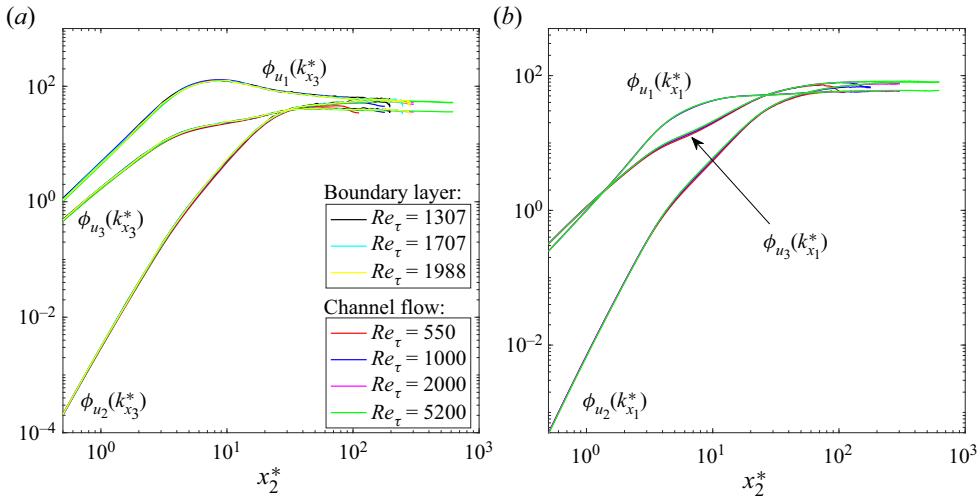


Figure 9. Energy spectra in a boundary layer and a channel flow. (a) Distributions of $\phi_{u_1}(k_{x_3}^*)$, $\phi_{u_2}(k_{x_3}^*)$ and $\phi_{u_3}(k_{x_3}^*)$ versus x_2^* at $k_{x_3}^* = 0.08$. (b) Distributions of $\phi_{u_1}(k_{x_1}^*)$, $\phi_{u_2}(k_{x_1}^*)$ and $\phi_{u_3}(k_{x_1}^*)$ versus x_2^* at $k_{x_1}^* = 0.06$. The plots use the wall-parameter-normalized spectra in a boundary layer (Simens *et al.* 2009; Jiménez *et al.* 2010; Borrell *et al.* 2013; Sillero *et al.* 2013) and the non-normalized spectra in a channel flow (Lee & Moser 2015, 2019). Note that the spectrum of u_1 at $Re_\tau = 550$ is not shown in (a,b) for the reason mentioned in the context of figure 6. Note also that when data were not obtained at exactly $k_{x_3}^* = 0.08$ and $k_{x_1}^* = 0.06$, interpolation was used, based on available spectra closest to these two locations.

extend to $k_{x_3}^* \approx 0.03$, 0.02 and 0.02 , respectively; note that $k_{x_3}^* \approx 0.02$ for $\phi_{u_2}(k_{x_3}^*)$ actually corresponds to $k_{x_3}^* \approx 0.04$ since the distributions of $\phi_{u_2}(k_{x_3}^*)$ are shifted to the left by 0.5 of a decade for clarity (see the caption of figure 7). A similar observation can be made for $\phi_{u_1}(k_{x_1}^*)$, $\phi_{u_2}(k_{x_1}^*)$ and $\phi_{u_3}(k_{x_1}^*)$ at $x_2^* = 50$ in figure 8(b), which shows that the collapse can be observed over the range $k_{x_1}^* \gtrsim 0.01$ – 0.03 when $Re_\tau \gtrsim 1000$. It is worth mentioning that the collapse of $\phi_{u_1}(k_{x_1}^*)$ at $x_2^* = 10$ in figure 8(a) can extend to $k_{x_1}^* \approx 0.001$, which is three decades larger than the Kolmogorov scales. It is clear that the wavenumber range over which the energy spectra collapse may depend not only on the specific small-scale quantity, but also on the location x_2^* . Another feature of figures 7 and 8 is that the collapse extends to increasingly smaller wavenumbers (larger scales) with increasing Re_τ , except for $\phi_{u_2}(k_{x_1}^*)$ at $x_2^* = 10$ (figure 8a), which collapses at all wavenumbers in the present Re_τ range. We recall that there is a strong departure from local isotropy in the context of the dissipation tensor in the region $x_2^* \lesssim 30$ (figure 3b). It is pertinent to identify the scales that characterize the anisotropy of $\bar{\epsilon}$. Although not shown here, at $x_2^* = 10$, the peaks of the dissipation spectra $k_{x_3}^{*2}\phi_{u_1}(k_{x_3}^*)$, $k_{x_3}^{*2}\phi_{u_2}(k_{x_3}^*)$ and $k_{x_3}^{*2}\phi_{u_3}(k_{x_3}^*)$ are located at $k_{x_3}^* \approx 0.11$, 0.19 and 0.09 , respectively. On the other hand, a general definition of the Taylor microscale is $\lambda = (5\nu)^{1/2} \overline{u_i u_i}^{1/2} / \bar{\epsilon}^{1/2}$. The estimated magnitude of λ/η is 11.7 – 12.8 at $x_2^* = 10$ in the channel flow for $Re_\tau = 550$ – 5200 . Therefore, the locations of the peaks of the dissipation spectra are comparable to λ . Namely, the anisotropy of $\bar{\epsilon}$ represents mainly the anisotropy of the scales around λ , at least at $x_2^* = 10$.

Further, according to (2.1), the energy spectra should depend only on the location x_2^* at a given small scale k^* . In order to demonstrate this, we report in figure 9(a) the distributions of $\phi_{u_1}(k_{x_3}^*)$, $\phi_{u_2}(k_{x_3}^*)$ and $\phi_{u_3}(k_{x_3}^*)$ versus x_2^* in a channel flow and a boundary layer at a typical $k_{x_3}^*$ ($= 0.08$). Similarly, figure 9(b) shows the distributions of $\phi_{u_1}(k_{x_1}^*)$, $\phi_{u_2}(k_{x_1}^*)$ and

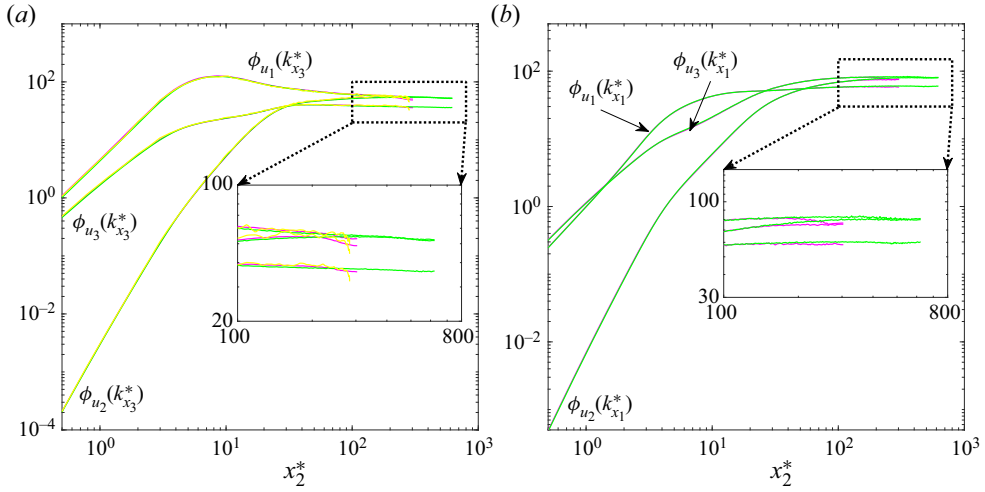


Figure 10. Energy spectra in a boundary layer and a channel flow corresponding to figures 9(a,b) for only $Re_\tau \gtrsim 2000$. The insets zoom in on the range $x_2^* = 100\text{--}800$.

$\phi_{u_3}(k_{x_1}^*)$ versus x_2^* in a channel flow at a typical $k_{x_1}^* (= 0.06)$. Evidently, there is reasonably good collapse in the near-wall regions and, generally, the larger Re_τ , the wider the x_2^* range over which the collapse occurs. In order to quantify the x_2^* range over which the spectra collapse at large Re_τ , we report in figures 10(a,b) the energy spectra corresponding to figures 9(a,b) for only $Re_\tau \gtrsim 2000$. It is clear that the collapse can extend to $x_2^* \approx 200$ for $Re_\tau \gtrsim 2000$ in a boundary layer and a channel flow. Overall, figures 5(b) and 6–10 provide good support for the present hypothesis in the context of energy spectra.

Finally, we test the hypothesis in the context of the transport equations for $\bar{\varepsilon}$ and $\bar{\varepsilon}_\theta$ in a channel flow:

$$\begin{aligned}
 & \underbrace{-\frac{\partial}{\partial x_2} \overline{u_2 \varepsilon}}_{T_u} - 2\nu \underbrace{\frac{\partial u_i}{\partial x_2} \frac{\partial u_i}{\partial x_1} \frac{\partial \bar{U}_1}{\partial x_2}}_{P_U} - 2\nu \underbrace{\frac{\partial u_1}{\partial x_k} \frac{\partial u_2}{\partial x_k} \frac{\partial \bar{U}_1}{\partial x_2}}_{P_m} - 2\nu \underbrace{\frac{\partial u_i}{\partial x_k} \frac{\partial u_l}{\partial x_k} \frac{\partial u_l}{\partial x_1}}_{P_u} \\
 & \underbrace{- 2\nu u_2 \frac{\partial u_1}{\partial x_2} \frac{\partial^2 \bar{U}_1}{\partial x_2 \partial x_2}}_{P_g} - 2\nu \underbrace{\frac{\partial}{\partial x_2} \frac{\partial u_2}{\partial x_k} \frac{\partial p}{\partial x_k}}_{\Pi} - 2\nu^2 \underbrace{\frac{\partial^2 u_i}{\partial x_k \partial x_l} \frac{\partial^2 u_i}{\partial x_k \partial x_l}}_D + \underbrace{\nu \frac{\partial^2 \bar{\varepsilon}}{\partial x_2^2}}_{T_v} = 0,
 \end{aligned} \tag{3.2}$$

$$\begin{aligned}
 & \underbrace{\frac{1}{Pr} \frac{\partial \overline{u_2 (\partial \theta / \partial x_i)^2}}{\partial x_2}}_{T_{\theta u}} - \underbrace{\frac{2}{Pr} \frac{\partial \theta}{\partial x_i} \frac{\partial \theta}{\partial x_j} \frac{\partial u_j}{\partial x_i}}_{P_{\theta u}} - \underbrace{\frac{2}{Pr} \frac{\partial \theta}{\partial x_2} \frac{\partial \theta}{\partial x_1} \frac{\partial \bar{U}_1}{\partial x_2}}_{P_{\theta U}} - \underbrace{\frac{2}{Pr} \frac{\partial \theta}{\partial x_i} \frac{\partial u_2}{\partial x_i} \frac{\partial \Theta}{\partial x_2}}_{P_{\theta \Theta}} \\
 & \underbrace{- \frac{2}{Pr} u_2 \frac{\partial \theta}{\partial x_2} \frac{\partial^2 \Theta}{\partial x_2 \partial x_2}}_{P_{\theta g}} - \underbrace{\frac{2}{Pr^2} \frac{\partial^2 \theta}{\partial x_j \partial x_i} \frac{\partial^2 \theta}{\partial x_j \partial x_i}}_{D_\theta} + \underbrace{\frac{1}{Pr^2} \frac{\partial^2 \bar{\varepsilon}_\theta}{\partial x_2^2}}_{T_\kappa} = 0,
 \end{aligned} \tag{3.3}$$

where \bar{U}_1 is the mean velocity in the streamwise (x_1) direction, and Θ is the mean scalar. In (3.2), the terms T_u , Π and T_v are the (large-scale) turbulent, pressure and

viscous diffusion terms, respectively. The terms P_U , P_m and P_g are the (large-scale) mixed production, mean gradient production and gradient production terms, respectively. The terms P_u and D are the small-scale terms that represent the production of $\bar{\varepsilon}$ through the stretching of vorticity, and its destruction through the action of viscosity, respectively. Similarly, in (3.3), terms $T_{\theta u}$ and T_κ are the (large-scale) turbulent and viscous diffusion terms, respectively. Terms $P_{\theta U}$, $P_{\theta\Theta}$ and $P_{\theta g}$ are the (large-scale) mixed production, mean gradient production and gradient production terms, respectively. Terms $P_{\theta u}$ and D_θ are the small-scale terms that represent the production of $\bar{\varepsilon}_\theta$ due to stretching of the temperature field and its destruction by the thermal diffusivity, respectively. All terms in (3.2), after normalizing by wall parameters (u_τ and ν) and Kolmogorov scales (η and u_K ; or equivalently, $\bar{\varepsilon}$ and ν), are shown in figures 11(a,b), respectively. It can be observed from figure 11(a) that the magnitudes of both large- and small-scale terms in the region near the wall increase with Re_τ , except for the gradient production term (P_g term) and the pressure term (Π term), which make only small contributions to (3.2). In contrast, the corresponding Kolmogorov-normalized distributions at $Re_\tau = 180$ and 590 (figure 11b) follow each other closely and, for $Re_\tau \gtrsim 590$, collapse reasonably well in the region $x_2^* \lesssim 60$. All terms in (3.3), after normalizing by the wall parameters (u_τ , θ_τ and ν) and the Batchelor–Kolmogorov scales (η , θ_B and u_K ; or equivalently, $\bar{\varepsilon}$, $\bar{\varepsilon}_\theta$ and ν), at $Pr = \nu/\kappa = 0.71$ and four values of Re_τ ($= 500, 1000, 2000, 5000$; the corresponding Péclet number is equal to $Re_\tau Pr$) are shown in figures 12(a,b). We can observe that there is a significant difference between the distributions normalized by wall parameters and those normalized by the Batchelor–Kolmogorov scales, for both large and small-scale terms. In the region near the wall, the magnitude of each term, normalized by wall parameters, increases systematically with Re_τ except for the gradient production term ($P_{\theta g}$ term), which makes only a small contribution to (3.3). However, the Batchelor–Kolmogorov normalized distributions collapse reasonably well in the region near the wall. As Re_τ increases, the x_2^* range for this collapse widens. Figures 11(b) and 12(b) provide further strong support for the present hypothesis.

4. Discussion

4.1. x_2^* range over which present hypothesis applies

It is of interest to identify the x_2^* range of validity for the present hypothesis. The following further comments can be made with regard to figures 4, 10, 11(b) and 12(b).

(i) Figure 4 shows that the distributions of R_i^* ($i = 1, 2, 3$) in a boundary layer collapse well with the channel data in the range $x_2^* \lesssim 70$ (or equivalently $x_2^+ \lesssim 213$ ($\approx 0.11\delta$) in the boundary layer at $Re_\tau = 1988$). In contrast, in the channel flow, the collapse of the R_i^* distributions at $Re_\tau = 2000$ and 5200 with the distribution at $Re_\tau = 10^4$ can extend to the channel centreline. A close look at the R_i^* distributions in the channel flow shows that the departure from the isotropic value of $2/3$ is smaller than 10 % and 5 % when $x_2^* \gtrsim 70$ and 150, respectively. Evidently, the channel flow approaches local isotropy gradually, which is a requirement of the KOC theory, with increasing x_2^* .

(ii) It can be observed from figures 10(a,b) that the collapse of the energy spectra at two typical scales ($k_{x_3}^* = 0.08$ and $k_{x_1}^* = 0.06$) can extend to $x_2^* \approx 200$ for $Re_\tau \gtrsim 2000$ in a boundary layer and a channel flow. At $Re_\tau \approx 2000$, $x_2^* \approx 200$ corresponds to $x_2^+ \approx 986$ ($\approx 0.49\delta$) in a channel flow and $x_2^+ \approx 795$ ($\approx 0.40\delta$) in a boundary layer. We should stress that the x_2^* range over which the energy spectra collapse can widen if we focus on a smaller

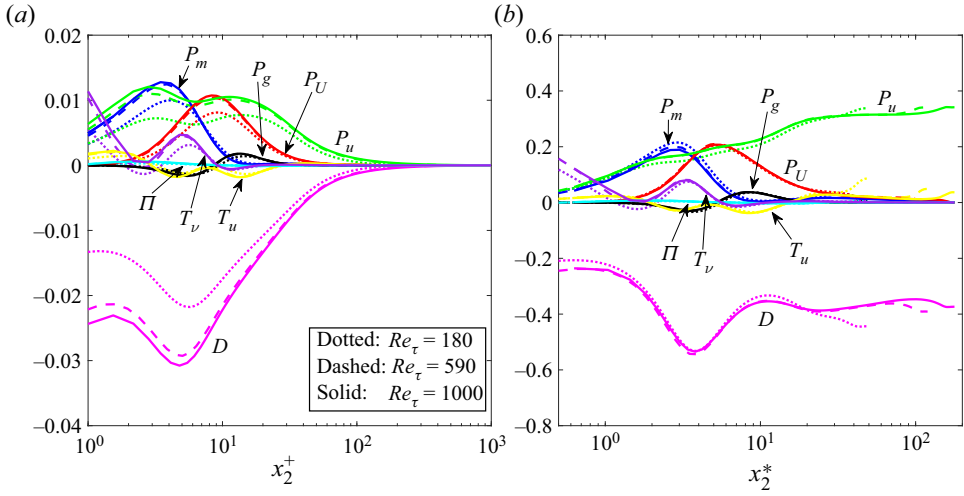


Figure 11. Distributions of terms in (3.2) in a channel flow. Normalizations based on (a) wall parameters and (b) Kolmogorov scales. They are plotted using the data of Vreman & Kuersten (2014a,b) and Kaneda & Yamamoto (2021). Note that for the data of Kaneda & Yamamoto (2021) at $Re_\tau = 1000$, there are two simulations with effective grid spacings $(\Delta x_1)^+ \times (\Delta x_2)^+ \times (\Delta x_3)^+ = 18.5 \times 0.6 - 0.8 \times 8.9$ and $7.8 \times 0.6 - 0.8 \times 4.2$. Only the latter dataset, corresponding to a higher resolution, is shown. Note that in order to obtain the Kolmogorov-normalized distributions in (b), the wall-parameter-normalized distributions in (a) are divided by $(u_K^+/\eta^+)^3$ since their relation in the context of transport equation for $\bar{\varepsilon}$ is given by [wall scaling] = [Kolmogorov scaling] $((u_K^4/\eta^2)(\delta_v^2/u_\tau^4))$ = [Kolmogorov scaling] (u_K^3/η^3) .

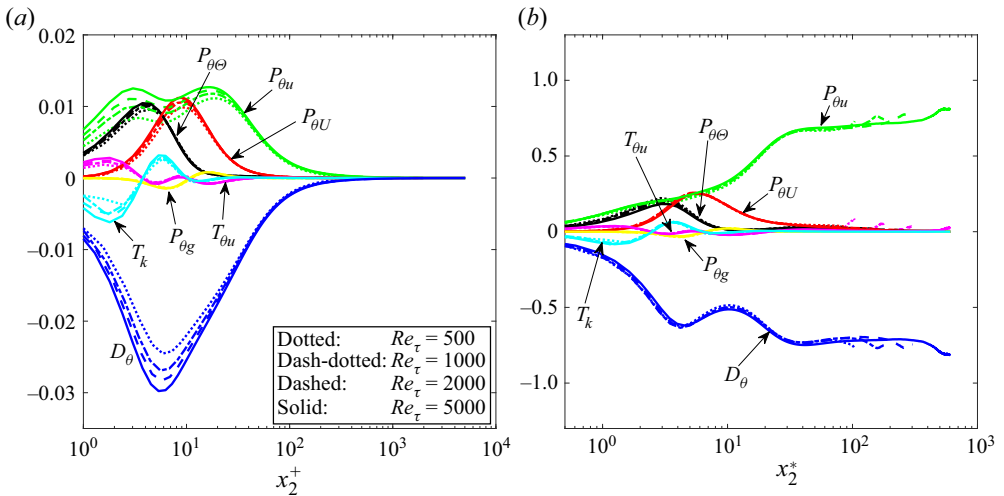


Figure 12. Distributions of terms in (3.3) for $Pr = 0.71$ in a channel flow. Normalizations based on (a) wall parameters and (b) Batchelor-Kolmogorov scales, using the information in Alcántara-Ávila *et al.* (2021), as explained in Appendix A.

scale (or larger wavenumber). In order to demonstrate this, we report in figure 13(a) the distributions of $\phi_{u_1}(k_{x_3}^*)$, $\phi_{u_2}(k_{x_3}^*)$ and $\phi_{u_3}(k_{x_3}^*)$ versus x_2^* in a channel flow at $k_{x_3}^* = 0.45$. We can observe that the collapse of the energy spectrum at $Re_\tau = 2000$ with the spectrum at $Re_\tau = 5200$ can extend to the channel centreline. In particular, in the region $x_2^* \gtrsim 60$,

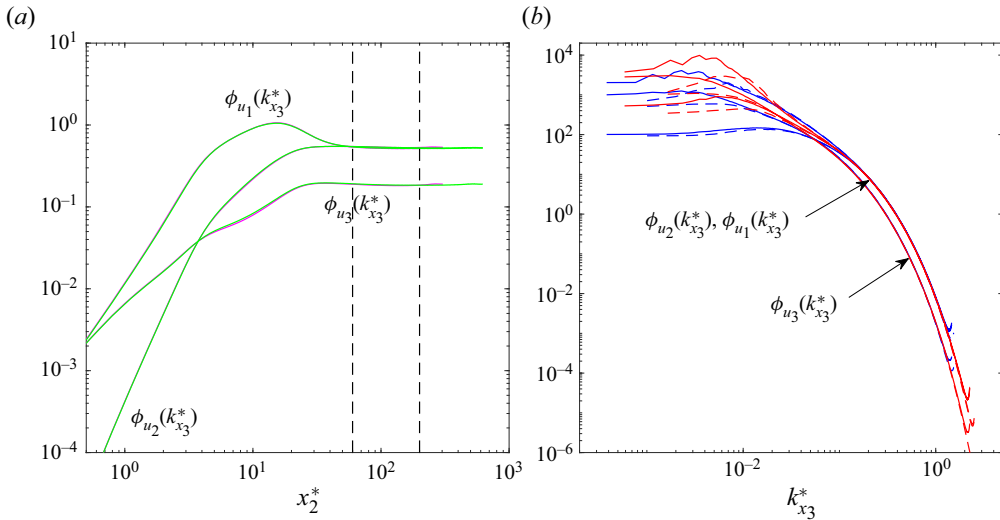


Figure 13. (a) Distributions of $\phi_{u_1}(k_{x_3}^*)$, $\phi_{u_2}(k_{x_3}^*)$ and $\phi_{u_3}(k_{x_3}^*)$ versus x_2^* in a channel flow at $k_{x_3}^* = 0.45$. Pink and green curves correspond to $Re_\tau = 2000$ and 5200 , respectively. The vertical lines indicate the locations at $x_2^* = 60$ and 200 , respectively. (b) Corresponding distributions of $\phi_{u_1}(k_{x_3}^*)$, $\phi_{u_2}(k_{x_3}^*)$ and $\phi_{u_3}(k_{x_3}^*)$ versus $k_{x_3}^*$ at $x_2^* = 60$ (blue curves) and 200 (red curves), respectively. Dashed and solid curves correspond to $Re_\tau = 2000$ and 5200 , respectively. They are plotted using the non-normalized spectra in a channel flow (Lee & Moser 2015, 2019).

all the spectra become approximately constant. This implies that beyond this location, the energy spectra depend only on the wavenumber (and not on x_2^*). Consequently, all the energy spectra in the region $x_2^* \gtrsim 60$ should collapse, which is the prediction of the KOC theory. This is indeed supported by figure 13(b), which shows the distributions of $\phi_{u_1}(k_{x_3}^*)$, $\phi_{u_2}(k_{x_3}^*)$ and $\phi_{u_3}(k_{x_3}^*)$ versus $k_{x_3}^*$ at two locations ($x_2^* = 60$ and 200) marked in figure 13(a); at $Re_\tau = 2000$, $x_2^* \approx 60$ and 200 correspond to $x_2^+ \approx 181$ ($\approx 0.09\delta$) and $x_2^+ \approx 985$ ($\approx 0.50\delta$), whereas at $Re_\tau = 5200$, $x_2^* \approx 60$ and 200 correspond to $x_2^+ \approx 179$ ($\approx 0.03\delta$) and $x_2^+ \approx 912$ ($\approx 0.18\delta$), respectively. This is also consistent with the collapse of the experimental data for $\phi_{u_1}(k_{x_1}^*)$ at various locations (away from the wall) in the pipe flow and the boundary layer at higher Re_τ (Rosenberg *et al.* 2013; Vallikivi *et al.* 2015). From the above discussion with respect to R_i^* and the energy spectra, it is obvious that the KOC theory represents a special case of the present hypothesis.

(iii) In figure 11(b), the collapse can be observed for all terms in (3.2) in the region $x_2^* \lesssim 60$ for $Re_\tau \gtrsim 590$. At $Re_\tau = 590$, $x_2^* \approx 50, 60$ and 80 correspond to $x_2^+ \approx 147$ ($\approx 0.25\delta$), $x_2^+ \approx 191$ ($\approx 0.32\delta$) and $x_2^+ \approx 296$ ($\approx 0.50\delta$), respectively.

(iv) In figure 12(b), the collapse of all terms in (3.3) can extend to $x_2^* \approx 85, 140$ and 240 for $Re_\tau \gtrsim 500, 1000$ and 2000 , respectively. The corresponding x_2^+ values are 342 ($\approx 0.68\delta$), 662 ($\approx 0.66\delta$) and 1360 ($\approx 0.68\delta$) at $Re_\tau = 500, 1000$, and 2000 , respectively. From the above results, it is remarkable that the x_2^* range over which the hypothesis is valid extends generally from the wall to a location in the outer region for the small-scale quantities examined here. This x_2^* range depends on the specific small-scale quantity. Generally, for a given small-scale quantity, the larger the Reynolds number, the wider the x_2^* range over which this quantity is Re_τ -independent.

4.2. Relationships to wall scaling and outer scaling for small-scale quantities

As pointed out in the context of figure 1, the collapse of $x_2^+ \bar{\varepsilon}^+$ over a certain x_2^+ range implies that the wall parameters and the Kolmogorov scales can be used interchangeably in this x_2^+ range in the channel flow. This can be extended in a more general way. If $x_2^+ \bar{\varepsilon}^+$ and $x_2^+ \bar{\varepsilon}_\theta^+$ can collapse onto unique curves in all turbulent wall flows over a certain x_2^+ range – which has not yet been established – then it is not difficult to conclude that the wall parameters and the Kolmogorov–Batchelor scales can be used interchangeably. However, if different wall flows have different Re_τ -independent $x_2^+ \bar{\varepsilon}^+$ (and $x_2^+ \bar{\varepsilon}_\theta^+$) distributions at large Re_τ , unlike the Kolmogorov–Batchelor normalized distributions, which are universal as shown in our paper, then the wall-parameter-normalized distributions should collapse onto different curves in different wall flows.

The same remark can be made with regard to the relationship between normalizations based on Kolmogorov–Batchelor and outer scales. In particular, it should be mentioned that if there is an overlap between the wall parameters scaling and outer scaling in the context of $\bar{\varepsilon}$ (Abe & Antonia 2016) (and also $\bar{\varepsilon}_\theta$; Abe & Antonia 2017), then at least for a given flow, all three types of scaling, i.e. the Kolmogorov–Batchelor scales, wall parameters and outer scales, can be used interchangeably. However, when the Kolmogorov–Batchelor normalized small-scale quantities are independent of x_2^* , such as the energy spectra at large x_2^* discussed in the context of figure 13, the outer scales and the Kolmogorov–Batchelor scales can be interchanged only when $\bar{\varepsilon} \delta / u_\tau^3$ (and also $\bar{\varepsilon}_\theta \delta / (u_\tau \theta_\tau^2)$) is constant (independent of x_2 / δ). Similarly, when the Kolmogorov–Batchelor normalized small-scale quantities are independent of x_2^* , the wall parameter and the Kolmogorov–Batchelor scales are interchangeable when $\bar{\varepsilon}^+$ (and also $\bar{\varepsilon}_\theta^+$) is constant (independent of x_2^+).

4.3. Behaviour of $\overline{u_i u_i}^*$ and $\overline{\theta \theta}^*$ as $x_2^* \rightarrow 0$

The present hypothesis has been proposed for small-scale quantities in wall turbulence and thus does not require $\overline{u_i u_i}^*$ and $\overline{\theta \theta}^*$ to be universal. However, in the region $x_2^* \rightarrow 0$, $\overline{u_i u_i}$ and $\overline{\theta \theta}$ are related directly to $\bar{\varepsilon}$ and $\bar{\varepsilon}_\theta$ (e.g. Pope 2000; Alcántara-Ávila *et al.* 2021), i.e.

$$\bar{\varepsilon} = \frac{1}{2} \nu \frac{\partial^2 \overline{u_i u_i}}{\partial x_2^2}, \quad \bar{\varepsilon}_\theta = \frac{1}{2} \kappa \frac{\partial^2 \overline{\theta \theta}}{\partial x_2^2}. \tag{4.1a,b}$$

One thus expects $\overline{u_i u_i}^*$ and $\overline{\theta \theta}^*$ to be universal as $x_2^* \rightarrow 0$. After normalization by the Batchelor–Kolmogorov scales, (4.1a,b) can be rewritten as

$$\frac{\partial^2 \overline{u_i u_i}^*}{\partial x_2^{*2}} = 2, \quad \frac{1}{Pr} \frac{\partial^2 \overline{\theta \theta}^*}{\partial x_2^{*2}} = 2. \tag{4.2a,b}$$

Note that we have assumed u_K , η and θ_B to be approximately constant as $x_2^+ \rightarrow 0$. These assumptions are justifiable. For example, figure 3 of Antonia *et al.* (1991) indicates that η^+ is approximately constant for $x_2^+ = 0.1-1$ at $Re_\tau = 180$ and 395, respectively. Although not shown here, the distributions of η^+ , u_K^+ and θ_K^+ versus x_2^+ for the present channel data at $Re_\tau = 500-10^4$ indicate that they are approximately constant for $x_2^+ \lesssim 1$ at each Re_τ .

Scaling of small-scale wall turbulence

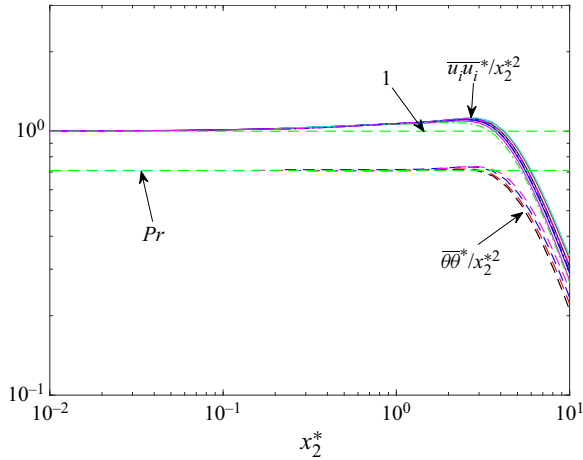


Figure 14. Distributions of $\overline{u_i u_i^*} / x_2^{*2}$ in a channel flow and a boundary layer. The solid pink, red, blue, black and cyan curves correspond to the channel data at $Re_\tau = 550, 1000, 2000, 5200$ and 10^4 , respectively. The dash-dotted green, blue and pink curves correspond to the boundary layer data at $Re_\tau = 445, 1307$ and 1988 , respectively. Also shown are the distributions of $\overline{\theta\theta^*} / x_2^{*2}$ in a channel flow; the dashed black, red, blue and pink curves correspond to $Re_\tau = 500, 1000, 2000$ and 5000 , respectively. They are plotted using the data of Simens *et al.* (2009), Jiménez *et al.* (2010), Borrell *et al.* (2013), Sillero *et al.* (2013), Lee & Moser (2015, 2019) and Alcántara-Ávila *et al.* (2021). The horizontal lines indicate the values of 1 and $Pr (= 0.71)$.

Integrating (4.2a,b) twice with respect to x_2^* leads to

$$\overline{u_i u_i^*} = x_2^{*2}, \quad \overline{\theta\theta^*} = Pr x_2^{*2}. \quad (4.3a,b)$$

Figure 14 shows that both $\overline{u_i u_i^*}$ and $\overline{\theta\theta^*}$ are independent of Re_τ in the range $x_2^* \lesssim 1$. In particular, (4.3a,b) are satisfied adequately in the region $x_2^* \lesssim 0.2$ for $\overline{u_i u_i^*}$ and $x_2^* \lesssim 1$ for $\overline{\theta\theta^*}$.

5. Concluding remarks

We have proposed a hypothesis that describes the behaviour of small-scale wall turbulence reasonably well. The evidence presented indicates that the larger the Reynolds number, the larger the distance from the wall and the range of turbulent scales over which this hypothesis applies. More specifically, at a given x_2^* , collapse of a given small-scale quantity generally extends to increasingly larger values of r^* (or smaller wavenumbers) as the Reynolds number increases. Similarly, the collapse of a given small-scale quantity extends to increasingly larger values of x_2^* as the Reynolds number increases. We stress that the present hypothesis has been tested and validated mainly in a channel flow and a boundary layer using a relatively large amount of data related mainly to second-order statistics. Direct numerical simulations (DNS) data corresponding to third-order statistics (figure 11b) also support the hypothesis. It is now desirable to test the hypothesis against other third- and higher-order statistics, e.g. the third- and fourth-order moments of different velocity derivatives. The statistics examined here have validated adequately the claim of independence with respect to Re_τ . Unfortunately, the data have been obtained mainly in two smooth wall flows (the channel and the boundary layer). It would certainly be desirable to test the hypothesis further in a fully developed pipe flow, preferably using DNS data where Re_τ exceeds 500, and more generally in flows over different types of surfaces.

The present hypothesis should greatly reduce the complexity of wall turbulence and also enhance our understanding of the physical mechanisms in wall flows. We should underline that an important application of the hypothesis is the ability to describe adequately the behaviour of small-scale quantities in wall turbulence. The collapse of the small-scale statistics shown in figures 4, 5(b), 6–10, 11(b), 12(b) and 13 suggests that the present hypothesis will underpin future developments of new wall turbulence models and thus should lead to a significant improvement in wall turbulence calculations. Since the accuracy of the hypothesis can only improve as Re_τ keeps increasing, calculations based on this hypothesis should be especially suitable in the context of very-large-Reynolds-number engineering and meteorological flows. Finally, a significant amount of evidence has shown that the present hypothesis is valid for small-scale velocity quantities in wall turbulence. In view of the similarity between the small-scale velocity and scalar ($Pr \approx 1$) fields (e.g. Abe *et al.* 2009; Antonia *et al.* 2009), one would expect that the present hypothesis will also be satisfied by small-scale scalar quantities in wall turbulence. The collapse in figure 12(b) is encouraging in this respect and should spawn future investigations.

Acknowledgements. We are grateful to all the authors cited in our figures for sharing their data.

Funding. S.L.T. wishes to acknowledge support given to him from NSFC through grants 11702074 and 91952109 and from the Research Grants Council of Shenzhen Government through grant RCYX20210706092046085.

Declaration of interests. The authors report no conflict of interest.

Author ORCIDs.

© S.L. Tang <https://orcid.org/0000-0001-6379-8505>.

Appendix A. Normalization of figure 12(b)

The relation between Batchelor–Kolmogorov scaling and wall scaling in the context of the transport equation for $\bar{\varepsilon}_\theta$ is given by

$$\begin{aligned}
 [\text{Batchelor–Kolmogorov scaling}] &= [\text{wall scaling}] \frac{u_\tau^4 \theta_\tau^2}{v^3} \frac{v^3}{u_K^4 \theta_B^2} \\
 &= [\text{wall scaling}] \frac{u_\tau^4 \theta_\tau^2}{u_K^4 \theta_B^2} = [\text{wall scaling}] \frac{u_\tau^4 \theta_\tau^2}{u_K^4 \bar{\varepsilon}_\theta \eta / u_K} = [\text{wall scaling}] \frac{u_\tau^4 \theta_\tau^2}{u_K^3 \bar{\varepsilon}_\theta \eta} \\
 &= [\text{wall scaling}] \frac{u_\tau^4 \theta_\tau^2}{u_K^2 \bar{\varepsilon}_\theta v} = [\text{wall scaling}] \frac{u_\tau \theta_\tau^2}{\bar{\varepsilon}_\theta \delta_v} \frac{u_\tau^2}{u_K^2} = [\text{wall scaling}] \frac{u_\tau \theta_\tau^2}{\bar{\varepsilon}_\theta \delta_v} \frac{\eta^2}{\delta_v^2} \\
 &= \frac{[\text{wall scaling}]}{\bar{\varepsilon}_\theta^+} \frac{\eta^2}{\delta_v^2} = \frac{[\text{wall scaling}]}{\bar{\varepsilon}_\theta^+ \sqrt{\bar{\varepsilon}^+}}, \tag{A1}
 \end{aligned}$$

where $+$ denotes normalization by u_τ , θ_τ and v . In order to obtain the Batchelor–Kolmogorov normalized transport equation for $\bar{\varepsilon}_\theta$ (3.3), the wall-parameter-normalized distributions of Alcántara-Ávila *et al.* (2021) (see also figure 12a) are divided by $\bar{\varepsilon}_\theta^+ \sqrt{\bar{\varepsilon}^+}$, as shown in figure 12(b).

Note that the values of $\bar{\varepsilon}^+$ for the data in figure 12(b) are not available. However, there are at least four datasets for $\bar{\varepsilon}^+$ at nearly the same Re_τ ($\approx 500, 1000, 2000$ and 5000); they are those of Bernardini, Pirozzoli & Orlandi (2014) ($Re_\tau = 550, 1000$ and 2000), Hoyas & Jimenez (2006, 2008) ($Re_\tau = 550, 950$ and 2000), Lee & Moser (2015, 2019)

Scaling of small-scale wall turbulence

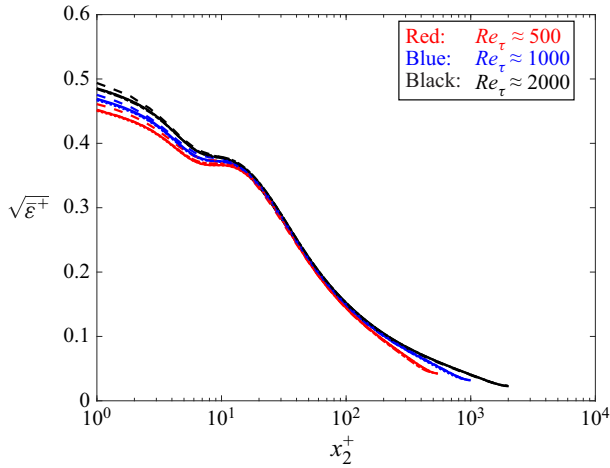


Figure 15. Distributions of $\sqrt{\bar{\varepsilon}^+}$ in a channel flow. The dashed, dotted, solid and dash-dotted curves correspond to the data of Bernardini *et al.* (2014) ($Re_\tau = 550, 1000$ and 2000), Hoyas & Jimenez (2006, 2008) ($Re_\tau = 550, 950$ and 2000), Lee & Moser (2015, 2019) ($Re_\tau = 550, 1000$ and 2000) and Kaneda & Yamamoto (2021) ($Re_\tau = 500, 1000$ and 2000), respectively.

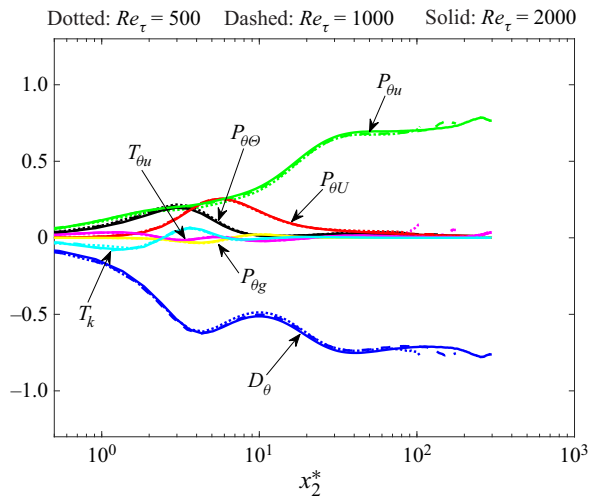


Figure 16. Batchelor–Kolmogorov normalized (3.3) at $Pr = 0.71$ in a channel flow. Note that the $\bar{\varepsilon}^+$ distributions of Bernardini *et al.* (2014) at $Re_\tau = 550, 950$ and 2000 are used for normalization.

($Re_\tau = 550, 1000, 2000$ and 5000) and Kaneda & Yamamoto (2021) ($= 500, 1000$ and 2000) (figure 15). It can be observed that there is only a small difference between the data of Bernardini *et al.* (2014) and the other three datasets at $Re_\tau \approx 550, 1000$ and 2000 , respectively; the difference between the dashed and dotted curves, which is maximum at $x_2^+ = 1$ and $Re_\tau = 550$, is only 2.3%. Therefore, the use of a different $\bar{\varepsilon}^+$ distribution will not affect the results in figure 12(b) where the $\bar{\varepsilon}^+$ distributions of Lee & Moser (2015, 2019) are used. This is supported by figure 16, which is normalized by the $\bar{\varepsilon}^+$ data of Bernardini *et al.* (2014) at $Re_\tau = 550, 1000$ and 2000 .

REFERENCES

- ABE, H. & ANTONIA, R.A. 2016 Relationship between the energy dissipation function and the skin friction law in a turbulent channel flow. *J. Fluid Mech.* **798**, 140–164.
- ABE, H. & ANTONIA, R.A. 2017 Relationship between the heat transfer law and the scalar dissipation function in a turbulent channel flow. *J. Fluid Mech.* **830**, 300–325.
- ABE, H., ANTONIA, R.A. & KAWAMURA, H. 2009 Correlation between small-scale velocity and scalar fluctuations in a turbulent channel flow. *J. Fluid Mech.* **627**, 1–32.
- ALCÁNTARA-ÁVILA, F., HOYAS, S. & PÉREZ-QUILES, M.J. 2021 Direct numerical simulation of thermal channel flow for $Re_\tau = 5000$ and $Pr = 0.71$. *J. Fluid Mech.* **916**, A29.
- ANTONIA, R.A., ABE, H. & KAWAMURA, H. 2009 Analogy between velocity and scalar fields in a turbulent channel flow. *J. Fluid Mech.* **628**, 241–268.
- ANTONIA, R.A. & KIM, J. 1994 Low-Reynolds-number effects on near-wall turbulence. *J. Fluid Mech.* **276**, 61–80.
- ANTONIA, R.A., KIM, J. & BROWNE, L.W.B. 1991 Some characteristics of small-scale turbulence in a turbulent duct flow. *J. Fluid Mech.* **233**, 369–388.
- BERNARDINI, M., PIROZZOLI, S. & ORLANDI, P. 2014 Velocity statistics in turbulent channel flow up to $Re_\tau = 4000$. *J. Fluid Mech.* **742**, 171–191.
- BORRELL, G., SILLERO, J.A. & JIMÉNEZ, J. 2013 A code for direct numerical simulation of turbulent boundary layers at high Reynolds numbers in BG/P supercomputers. *Comput. Fluids* **80**, 37–43.
- CHASSAING, P., ANTONIA, R.A., ANSELMET, F., JOLY, L. & SARKAR, S. 2002 *Variable Density Fluid Turbulence*. Kluwer Academic Publishers.
- CORRSIN, S. 1951 On the spectrum of isotropic temperature fluctuations in an isotropic turbulence. *J. Appl. Phys.* **22**, 469–473.
- GEROLYMOS, G.A. & VALLET, I. 2016 The dissipation tensor ε_{ij} in wall turbulence. *J. Fluid Mech.* **807**, 386–418.
- HOYAS, S. & JIMENEZ, J. 2006 Scaling of the velocity fluctuations in turbulent channels up to $Re_\tau = 2003$. *Phys. Fluids* **18**, 011702.
- HOYAS, S. & JIMENEZ, J. 2008 Reynolds number effects on the Reynolds-stress budgets in turbulent channels. *Phys. Fluids* **20**, 101511.
- HOYAS, S., OBERLACK, M., ALCÁNTARA-ÁVILA, F., KRAHEBERGER, S.V. & LAUX, J. 2022 Wall turbulence at high friction Reynolds numbers. *Phys. Rev. Fluids* **7**, 014602.
- JIMÉNEZ, J., HOYAS, S., SIMENS, M.P. & MIZUNO, Y. 2010 Turbulent boundary layers and channels at moderate Reynolds numbers. *J. Fluid Mech.* **657**, 335–360.
- KANEDA, Y. & YAMAMOTO, Y. 2021 Velocity gradient statistics in turbulent shear flow: an extension of Kolmogorov's local equilibrium theory. *J. Fluid Mech.* **929**, A13.
- KASAGI, N., TOMITA, Y. & KURODA, A. 1992 Direct numerical simulation of passive scalar field in a turbulent channel flow. *Trans. ASME J. Heat Transfer* **114**, 598–606.
- KOLMOGOROV, A.N. 1941 Local structure of turbulence in an incompressible fluid for very large Reynolds numbers. *Dokl. Akad. Nauk SSSR* **30**, 299–303.
- LEE, M. & MOSER, R.D. 2015 Direct numerical simulation of turbulent channel flow up to $Re_\tau = 5200$. *J. Fluid Mech.* **774**, 395–415.
- LEE, M. & MOSER, R.D. 2019 Spectral analysis of the budget equation in turbulent channel flows at high Reynolds number. *J. Fluid Mech.* **860**, 886–938.
- MARUSIC, I., MATHIS, R. & HUTCHINS, N. 2010 Predictive model for wall-bounded turbulent flow. *Science* **329** (5988), 193–196.
- NELKIN, M. 1992 In what sense is turbulence an unsolved problem? *Science* **255** (5044), 566–570.
- OBUKHOV, A.M. 1949 Structure of the temperature field in turbulent flows. *Izv. Akad. Nauk SSSR Geogr. Geofiz* **13**, 58–69.
- PIROZZOLI, S., ROMERO, J., FATICA, M., VERZICCO, R. & ORLANDI, P. 2021 One-point statistics for turbulent pipe flow up to $Re_\tau \approx 6000$. *J. Fluid Mech.* **926**, A28.
- POPE, S.B. 2000 *Turbulent Flows*. Cambridge University Press.
- PUMIR, A., XU, H. & SIGGIA, E.D. 2016 Small-scale anisotropy in turbulent boundary layers. *J. Fluid Mech.* **804**, 5–23.
- ROSENBERG, B.J., HULTMARK, M., VALLIKIVI, M., BAILEY, S.C.C. & SMITS, A.J. 2013 Turbulence spectra in smooth- and rough-wall pipe flow at extreme Reynolds numbers. *J. Fluid Mech.* **731**, 46–63.
- SADDOUGH, S.G. & VEERAVALLI, S.V. 1994 Local isotropy of turbulent boundary layers at high Reynolds number. *J. Fluid Mech.* **268**, 333–372.
- SCHUMACHER, J., SREENIVASAN, K.R. & YEUNG, P.K. 2003 Derivative moments in turbulent shear flows. *Phys. Fluids* **15**, 84–90.

Scaling of small-scale wall turbulence

- SHEN, X. & WARHAFT, Z. 2000 The anisotropy of the small scale structure in high Reynolds number ($Re_\lambda \sim 1000$) turbulent shear flow. *Phys. Fluids* **12**, 2976–2989.
- SILLERO, J.A., JIMÉNEZ, J. & MOSER, R.D. 2013 One-point statistics for turbulent wall-bounded flows at Reynolds numbers up to $\delta^+ \approx 2000$. *Phys. Fluids* **25** (10), 105102.
- SIMENS, M.P., JIMÉNEZ, J., HOYAS, S. & MIZUNO, Y. 2009 A high-resolution code for turbulent boundary layers. *J. Comput. Phys.* **228** (11), 4218–4231.
- SMITS, A.J. & MARUSIC, I. 2013 Wall-bounded turbulence. *Phys. Today* **66** (9), 25–30.
- TANG, S.L., ANTONIA, R.A., DJENIDI, L., ABE, H., ZHOU, T., DANAILA, L. & ZHOU, Y. 2015 Transport equation for the mean turbulent energy dissipation rate on the centreline of a fully developed channel flow. *J. Fluid Mech.* **777**, 151–177.
- VALLIKIVI, M., GANAPATHISUBRAMANI, B. & SMITS, A.J. 2015 Spectral scaling in boundary layers and pipes at very high Reynolds numbers. *J. Fluid Mech.* **771**, 303–326.
- VREMAN, A.W. & KUERTEN, J.G.M. 2014a Comparison of direct numerical simulation databases of turbulent channel flow at $Re_\tau = 180$. *Phys. Fluids* **26**, 015102.
- VREMAN, A.W. & KUERTEN, J.G.M. 2014b Statistics of spatial derivatives of velocity and pressure in turbulent channel flow. *Phys. Fluids* **26**, 085103.
- WARHAFT, Z. 2000 Passive scalars in turbulent flows. *Annu. Rev. Fluid Mech.* **32**, 203–240.